

고전도도 메탈메쉬가 적용된 낙뢰 손상 보호
샌드위치 스틸스 복합재 구조의 성능 평가

**Protection concept for foamed radar-absorbing sandwich composites
with high-conductive film against lightning strike impact**

Abstract

This paper presents a foamed radar-absorbing sandwich composite using Ni-plated glass fiber, serving as a dielectric loss material, and a high-conductive film for lightning strike protection. Image processing found that surface damage area was reduced by 38.7% in high-conductive films compared to those without. Furthermore, micro-X-ray CT revealed no critical damage, such as fiber breakage, deeper than the film. Moreover, specimens without high-conductive film experienced a 37.8% decrease in -10 dB bandwidth after the lightning strike test, while high-conductive film specimens maintained a -10 dB bandwidth. The proposed structure offers high radar absorbing performance, effectively protecting the structure from lightning.

Key Words : Functional composite; EM wave absorption; Lightning strike protection; Electrical Properties

1. Introduction

A multifunctional structure can simultaneously support loads and perform various functions. An example of a multifunctional structure is a radar-absorbing structure (RAS), which possesses load-bearing and radar-absorbing capabilities. Materials with semiconductor-like properties must be included in implementing an RAS. Composite materials involve two or more materials existing in different states, manipulating the properties of some constituent materials to achieve multifunctional structures. Therefore, research has been conducted using materials such as glass/epoxy or aramid/epoxy as a base, adding carbon nanotubes (CNT) to the matrix or coating fibers with metallic materials such as Ni to achieve the desired properties for RAS⁽¹⁻¹⁴⁾. However, the movement of atmospheric charges induces an electrical polarization between negative and positive poles, generating lightning⁽¹⁵⁾ and damaging buildings and structures. Aircraft are highly vulnerable to lightning strikes, with an average frequency of one strike per year⁽¹⁶⁻¹⁸⁾. With the increasing use of composite materials in aircraft, there is a growing need to understand the impact of lightning strikes on these materials, which has led to extensive research in this area⁽¹⁹⁻³⁵⁾. Feraboli et al. evaluated the extent of damage caused when lightning strikes were applied to carbon fiber-reinforced plastics (CFRP) with metal fasteners using techniques such as a C-scan⁽¹⁹⁾. Li et al. investigated the damage caused by lightning strikes based on the stacking method of unidirectional carbon-woven fabric/epoxy laminate⁽²⁰⁾. In addition, studies on composite material damage caused by lightning confirmed the occurrence of different damages. One of the causes of lightning-induced damage is high lightning voltage, which generates high heat when encountering materials with high resistance. This leads to resin evaporation and gas discharge, resulting in resin deterioration, delamination, and fiber breakage⁽³¹⁾. Ogasawara analytically confirmed the lightning damage caused by Joule heating and observed that the damage was greater in materials with high electric resistance⁽³⁵⁾. Therefore, measures are required to protect the composite materials using dielectric materials in RAS against lightning strikes. As shown in Table 1, previous research has focused on placing high-conductive

materials such as metal meshes, CNT, and conductive polymers on the outermost layers to protect the composite materials from lightning strikes⁽³⁶⁻⁴⁹⁾.

However, because highly conductive materials possess reflective properties, their application in RAS poses challenges⁽⁵⁰⁾. Thus, research focused on studying the extent of damage caused, changes in radar-absorbing performance, mechanical performance changes, and repair methods for lightning-damaged RAS rather than on protection against lightning-induced damage^(51, 52). This study proposes a foam radar-absorbing sandwich composite with a high-conductive film applied as a lightning strike protection configuration while maintaining radar-absorbing performance. The proposed structure is shown in Fig. 1. This structure comprises radar stealth functional and sacrificial protection components. The sacrificial protection component included a high-conductive film to protect the radar stealth functional component from lightning strikes. Impedance matching was achieved using Ni-plated glass fiber (NPF) and pristine glass fiber to maintain the radar-absorbing performance. Lightning strikes were applied to the proposed structure using a lightning impulse generator, and the lightning strike protection and radar-absorbing performances were confirmed through damage assessment.

Table 1: Reported lightning strike protection for composite materials

No.	Materials	Methods	Electric Conductivities	Notes
Ma et al ⁽³³⁾ .	MWNT	Dispersed in matrix	23,423 S/m (In-plane) 85.06 S/m (Out-of-plane)	Young's modulus: 79.59 GPa Shear modulus: 30.16 GPa
Kumar et al ⁽³⁴⁾ .	Polyaniline-based conductive resin	Conductive resin	9,031 S/m (In-plane) 110 S/m (Out-of-plane)	Three-point flexural test Flexural strength: 444 MPa (Residual strength: 92%)
Zhang et al ⁽³⁵⁾ .	MWNT/PEK-C film	Film	600 S/m	Damage area and depth reduction Damage area: 77.6% Damage depth: 68.0%
Guo et al ⁽³⁶⁾ .	AgNWs-loaded veil	Interleaf material	25,000 S/m (In-plane) 2,564 S/m (In-plane) 139 S/m (Out-of-plane)	Mode I and Mode II fracture toughness Mode I: 667 J/m ² Mode II: 2345 J/m ²
Wang et al ⁽³⁷⁾ .	Reduced graphene oxide (RGO)	Percolating-assisted resin film infusion method	44,000 S/m	Flexural strength: 469 MPa (Residual strength: 77%)

Chakravarthi et al ⁽³⁸⁾ .	Ni-coated SWNT	Sprayed on carbon ply	$2 \times 10^2 - 4 \times 10^2$ Ω/sq	-
Katunin et al ⁽³⁹⁾ .	PANI/epoxy	Conductive resin	18.4 ± 13.2 S/m	-
Rehbein et al ⁽⁴⁰⁾ .	Silver-coated polyamide yarn	Knitting	30,678 S/m (In-plane) 627.0 S/m (Out-of-plane)	Damage area reduction: 90%
Yokozeeki et al ⁽⁴¹⁾ .	PANI-based conductive polymer	Conductive resin	14,800 S/m (In-plane) 74 S/m (Out-of-plane)	-
Wang et al ⁽⁴²⁾ .	Aluminum coating	Sprayed coating	3,820,000 S/m	Ultrasonic C-scanning
Xia et al ⁽⁴³⁾ .	Silver modified buckypaper	Added onto the CFRP surface	509,165 S/m	Compression after a lightning strike Compressive strength: 284.08 MPa (Residual strength: 97.25%)
Zhu et al ⁽⁴⁴⁾	Nylon filter/nickel	Added onto the CFRP surface	31,700 S/m	Compression after a lightning strike Compressive strength: 208.71 MPa (Residual strength: 95.8%)
Lin et al ⁽⁴⁵⁾ .	MWNT, carbon black (CB)	Dispersed in matrix	-	Three-point flexural test Flexural strength: 478.73 MPa (Residual strength: 87.3%)
Chu et al ⁽⁴⁶⁾ .	Silver nanoparticles modified CNT paper	Added onto the CFRP surface	360,000 S/m	Three-point bending test Rupture load: 1795 N (Residual strength: 92.1%)

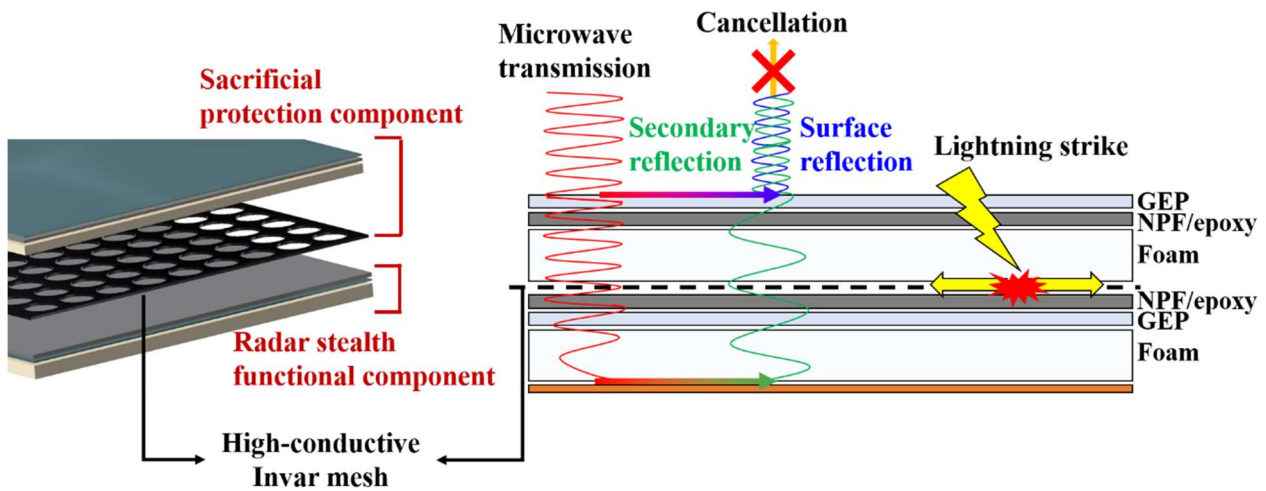


Fig. 1 Schematic of the foamed radar-absorbing sandwich composites with high-conductive film for lightning strike protection

2. Material and methods

2.1 Material preparations

This study used glass/epoxy prepreg (GEP 118, Minhu Composite Co., Ltd., South Korea), foam (Rohacell HF 71), and a high-conductive film (Invar 36 UNS K93600, Gang METAL, South Korea). Glass/epoxy was employed for load-bearing and impedance matching for the radar-absorbing performance, whereas foam served as a spacer. A high-conductive film for lightning-strike protection was fabricated using Invar. The thickness of the high-conductive film utilized was 0.102 mm, with an electrical conductivity of 1.25×10^6 S/m. The patterns were fabricated on high-conductive films using etching equipment. In addition, glass fibers plated with Ni with a thickness below the skin depth were utilized for load-bearing and impedance matching for radar-absorbing performance. The skin depth represents how deeply an electromagnetic field penetrates a specific material, indicating the depth at which the field strength decreases to $1/e$ (approximately 37%) when the electromagnetic field penetrates the material. Coating metallic materials with thicknesses greater than the skin depth results in properties of reflecting electromagnetic waves, whereas coating metal materials with thicknesses below the skin depth exhibits properties similar to those of dielectric lossy materials commonly used in RAS⁽⁵³⁾. The NPF used in this study were produced by plating glass fibers (Glass 1180, Hyundai Fiber Co., South Korea) with Ni using an electroless plating process at A-JINELECTRON Co., Ltd., as shown in Fig. 2(a). Fig. 2(c) shows the pristine glass fibers and NPF, as shown in Fig. 2(b), using a scanning electron microscope to confirm the presence of the Ni coating layer. Pristine glass fibers exhibit a smooth surface with no Ni particles, whereas NPF has a rough surface because of Ni particles. This characteristic indicates increased adhesion between the fiber and matrix when using NPF⁽⁵⁴⁾. Fig. 2(d) and Table 2 present the elemental compositions of the pristine glass fiber and NPF using energy-dispersive X-ray spectroscopy (EDS). Although Ni is not detected in pristine glass fibers, it is found in NPF at 4.45 wt% and 2.51 at%, indicating successful electroless plating of Ni. Fig. 2(e) shows the thickness of the Ni coating on the NPF obtained using EDS. With a thickness of 44.66 nm, thinner than the skin depth of Ni (1.33 μ m), NPF can be used as dielectric lossy materials for RAS.

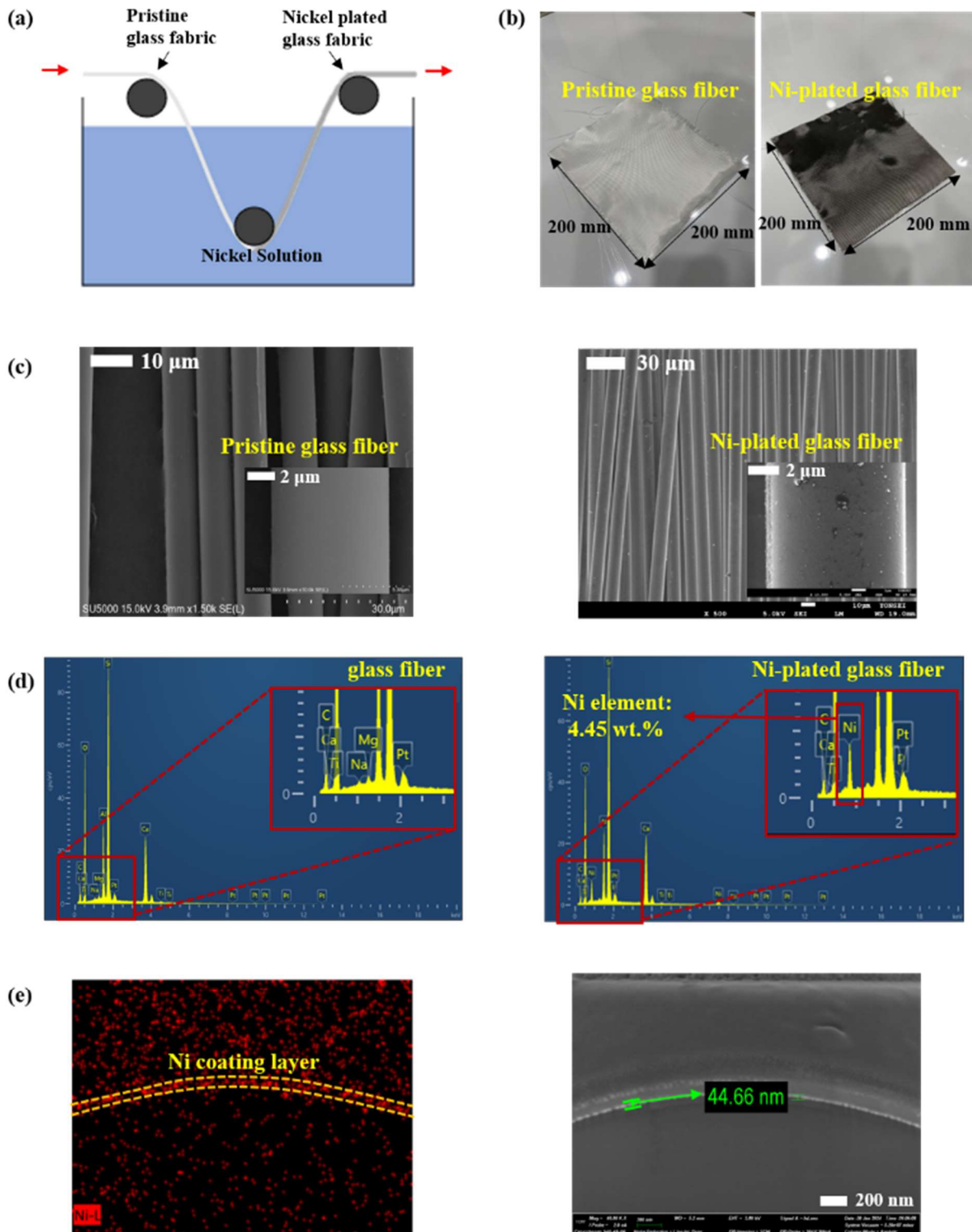


Fig. 2. (a) Nickel electroless plating method, (b) Pristine and nickel-plated glass fibers, (c) Scanning electron microscope and (d) Energy dispersive X-ray spectroscopy (EDS) results of pristine and nickel-plated glass fibers, (e) Nickel coating layer observed via EDS

Table 2: EDS elemental composition analysis of pristine and Ni-plated glass fiber composites.

Sample	wt.%/at.%					
	C	O	Al	Si	Ca	Ni
Pristine glass fiber	8.03/ 14.11	39.55/ 52.23	7.07/ 5.54	24.32/ 18.29	16.89/ 8.90	0.00/ 0.00
Ni-plated glass fiber	5.50/ 10.45	35.26/ 50.32	6.81/ 5.76	25.35/ 20.61	18.00/ 10.26	4.45/ 1.73

2.2 Dielectric properties

The electromagnetic properties of the materials are required for designing RAS. We prepared NPF/epoxy, glass/epoxy, and foam specimens, of which NPF and glass fibers were stacked by hand lay-up with epoxy (YD-128, Kukdo Chemical Co., South Korea) and a hardener (TH-431, Kukdo Chemical Co., South Korea), followed by autoclave curing. The fabricated NPF/epoxy, glass/epoxy, and foam were processed into a donut shape with an outer diameter of 7.00 mm and inner diameter of 3.04 mm to fit into a coaxial waveguide. The complex permittivity and permeability were measured using a network analyzer and coaxial waveguide, and the results for the measurement frequency range of 6 to 18 GHz are summarized in Fig. 3 and Table 3. Because the materials used in the study were dielectrics, the electromagnetic analysis was conducted with the complex permeabilities of the materials set to $1 - j0$. Based on the complex permittivity of NPF/epoxy, it was confirmed that NPF/epoxy is a lossy material that can be utilized in the design of RAS.

Table 3: Material properties for electromagnetic simulation

Materials	Electromagnetic Properties		Electric Properties
	Complex Permittivities (@10 GHz)	Complex Permeabilities (@10 GHz)	Electric Conductivities (S/m)
GFRP	4.57 - j0.05	0.92 - j0.01	-
NPF/epoxy	5.77 - j6.60	0.98 - j0.02	-
Foam	1.03 - j0.01	0.95 - j0.01	-
Invar	-	-	1.25×10^6

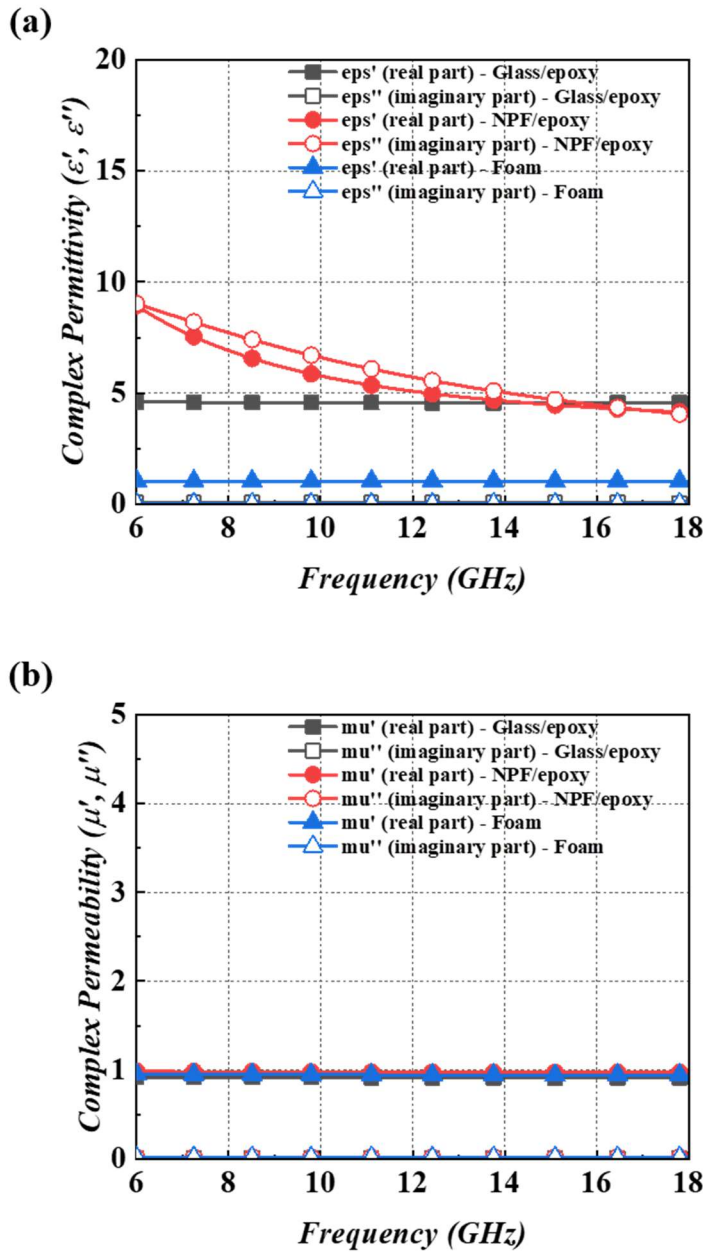


Fig. 3. (a) Complex permittivity and (b) Complex permeability of glass/epoxy, nickel-plated glass/epoxy, and foam

2.3 Lightning strike testing condition

The lightning strike tests were conducted in accordance with the MIL-STD-1757 standard⁽⁵⁵⁾. This standard categorizes lightning strike tests on specimen units into four components based on current intensity and duration: A (initial stroke), B (intermediate current), C (continuing current), and D (restrike). In this study, the test was conducted using the current waveform of component A, which has the highest current intensity. The waveform was controlled using parameters such as the peak current (I_{peak}), rise time (t_1), and decay time (t_2), as shown in Fig. 4(a). t_1 represents the time required for the current

intensity to reach 10–90% of the peak value, whereas t_2 represents the time required for the current intensity to increase from 10% of the peak value to surpass it and again reach 50% of the peak value.

Lightning strike tests were conducted using a lightning impulse generator (High-Voltage Laboratory, Mississippi State University), as shown in Fig. 4(b). A high-capacity impulse generator is required because of the low electrical conductivity of the RAS specimen used compared with that of metallic materials. An eight-capacitor setup was configured in parallel to create a lightning impulse generator capable of generating up to 400 kJ of lightning energy. A copper tape was applied to the bottom of the specimens used to test the electrical connections between the specimens and ground. The distance between the specimen and probe was set to 2 mm. The parameters of the A-component waveform were identified as $I_{peak} = 40 \text{ kA}$, $t_1 = 8 \text{ }\mu\text{s}$, and $t_2 = 20 \text{ }\mu\text{s}$.

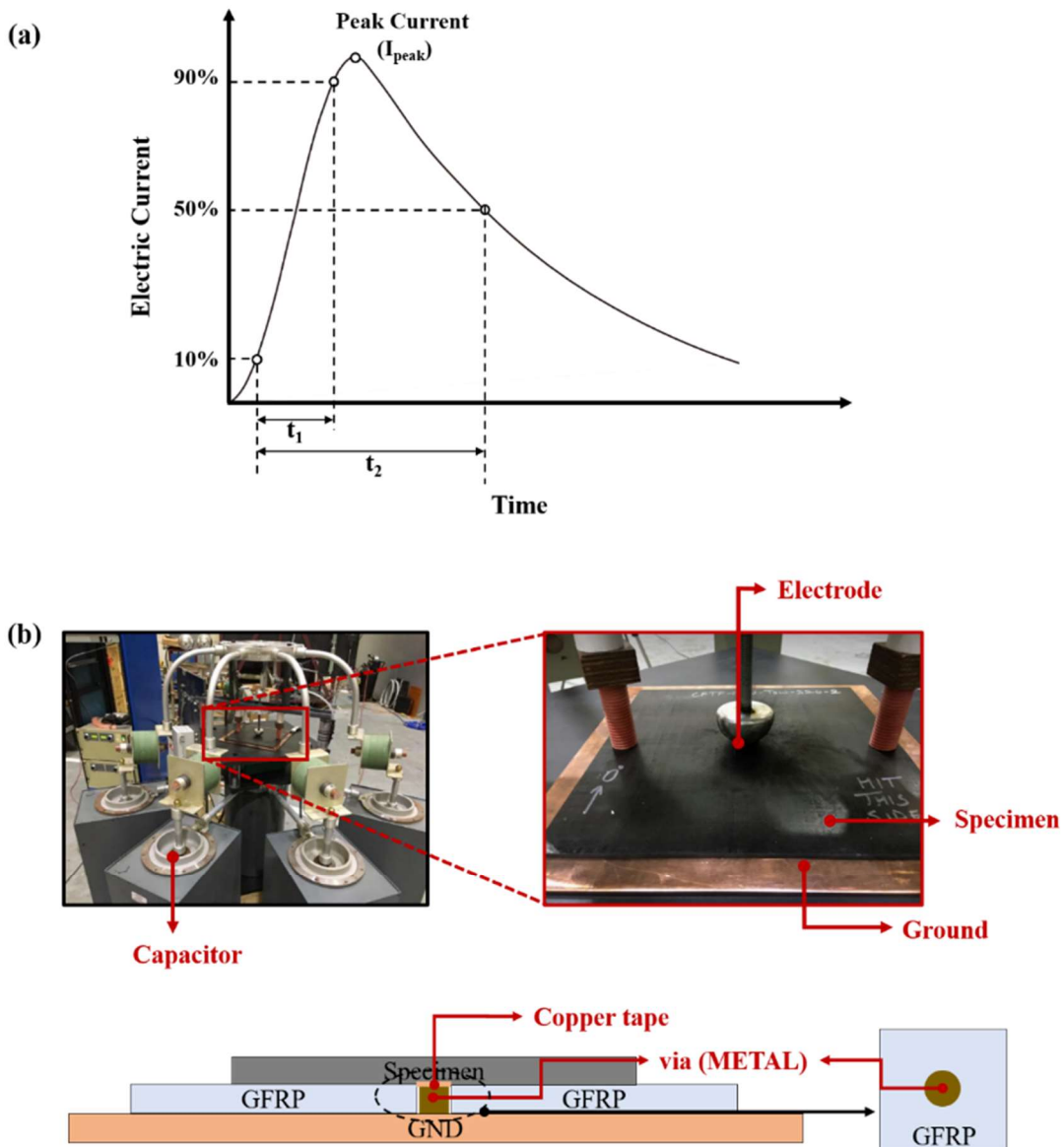


Fig. 4 (a) Parameters of current waveform A, (b) Lightning impulse generator and schematic of specimen setup

3. Design and fabrication

3.1 Design of foamed radar-absorbing sandwich composites

The foamed radar-absorbing sandwich composites were designed to maintain radar-absorbing performance even after the sacrificial protection component was damaged owing to a lightning strike. A foam radar-absorbing sandwich composite, including a patterned high-conductive film, was designed in two steps. First, a Dallenbach-type RAS without the high-conductive film was designed using the transmission line theory for the radar stealth functional component. Subsequently, RAS, comprising two slabs and a sacrificial protection component, was designed using an electromagnetic simulation tool and genetic algorithms.

Dallenbach-type RAS was designed using the measured electromagnetic properties and transmission line theory. This resonance-type RAS utilizes two or more materials and was designed by adjusting the material thickness. The reflection coefficient (R) of a Dallenbach-type RAS comprising n slabs, as shown in Fig. 5(a), can be expressed as follows:

$$R = \frac{Z_{in} - Z_0}{Z_{in} + Z_0} \quad (1)$$

where Z_{in} is the input impedance of the Dallenbach-type RAS and Z_0 is the characteristic impedance of air. Z_{in} is determined based on the complex permittivity, permeability, and thickness of each slab. The characteristic impedance Z_{ci} and propagation constant γ_i of the i -th slab can be calculated as follows:

$$Z_{ci} = Z_0 \sqrt{\frac{\mu_{ri}}{\epsilon_{ri}}} \quad (2)$$

$$\gamma_i = j \frac{2\pi}{\lambda} \sqrt{\epsilon_{ri} \mu_{ri}} \quad (3)$$

where μ_{ri} and ϵ_{ri} are the complex permeability and permittivity of the i -th slab, respectively, and λ is the wavelength. Then, the impedance of each slab can be calculated as follows:

$$Z_i = Z_{ci} \frac{Z_{i-1} + Z_{ci} \tanh(\gamma_i d_i)}{Z_{ci} + Z_{i-1} \tanh(\gamma_i d_i)} \quad (4)$$

where d_i is the thickness of i -th slab. Since there is a metallic material at the bottom of the resonance-type RAS, Z_0 is 0. The impedance of the n -th slab, Z_n , is the input impedance Z_{in} . By substituting the input and characteristic impedances of air into Eq. (1), the reflection efficiency of the RAS is calculated. Finally, the radar stealth functional component satisfying the condition of a reflection coefficient below -10 dB across the entire X-band was designed.

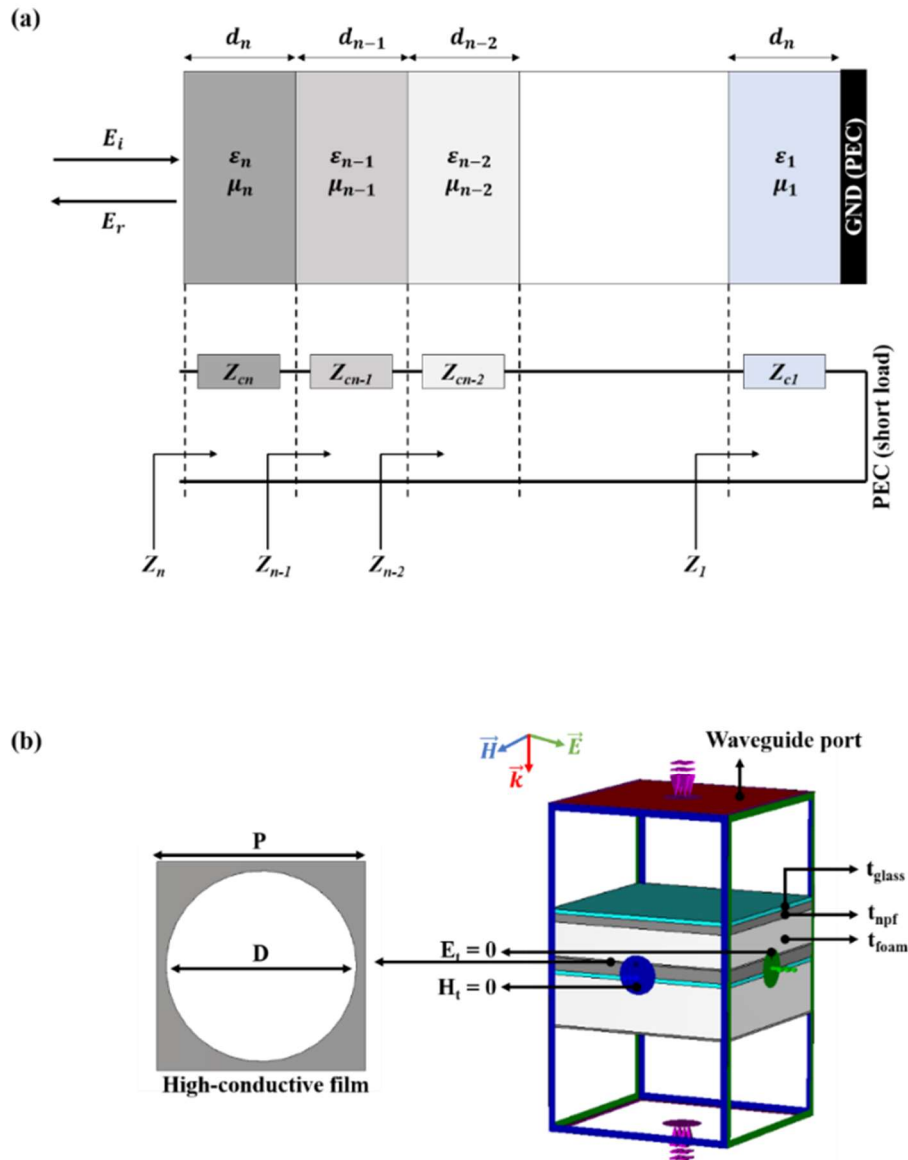


Fig. 5. (a) Transmission line model of Dallenbach-type RAS, (b) Unit-cell model of RAS with high-conductive film and design parameter

A sacrificial protection component using an electromagnetic simulation tool and a genetic algorithm was designed for foamed radar-absorbing sandwich composites incorporating lightning strike effects. Because the component includes a patterned high-conductive film, it has limitations when designed using a previous formula. CST Microwave Studio was utilized to verify the precise radar-absorbing performance. MATLAB was employed with a genetic algorithm to design foamed radar-absorbing sandwich composites, including a high-conductive film. A simulation model (Fig. 5(b)) validated the accurate radar-absorbing performance of the design. To expedite the simulation, the design was conducted utilizing the electric tangential field ($E_t = 0$) and magnetic tangential field ($H_t = 0$) boundary conditions and a unit cell model. The diameter of the pattern (D), periodicity of the pattern (P), and thickness of each layer were set as the design parameters. The radar stealth functional component utilized the same model as designed to ensure that the radar-absorbing performance was maintained even if the sacrificial protection component was removed due to a lightning strike. Data on the radar-

absorbing performance analyzed through CST Microwave Studio were transferred to MATLAB, and the optimization variables set in MATLAB were communicated to CST Microwave Studio to be reflected in the model, thus integrating the two programs. The design applied conditions ensuring radar-absorbing performance below -10 dB across the X-band, similar to the radar stealth functional component design.

Foamed radar-absorbing sandwich composites with a high-conductive film incorporating lightning strike protection performance, as shown in Fig. 6, have two components: a sacrificial protection component and radar stealth functional component, hence named double-slab foamed RAS with a lightning strike protection component (DFRL). Specimens without the high-conductive film were prepared to verify the lightning strike protection performance of the high-conductive films. The double-slab foamed RAS (DFR) is a foamed radar-absorbing sandwich composite without the high-conductive film, designed to ensure radar-absorbing performance below -10 dB across the entire C-band but not in the X-band due to its thick thickness. In addition, specimens of a single-slab foamed RAS (SFR) were prepared to verify the radar-absorbing performance of the radar stealth functional components. The stacking sequences for manufacturing DFRL, DFR, and SFR are summarized in Table 4.

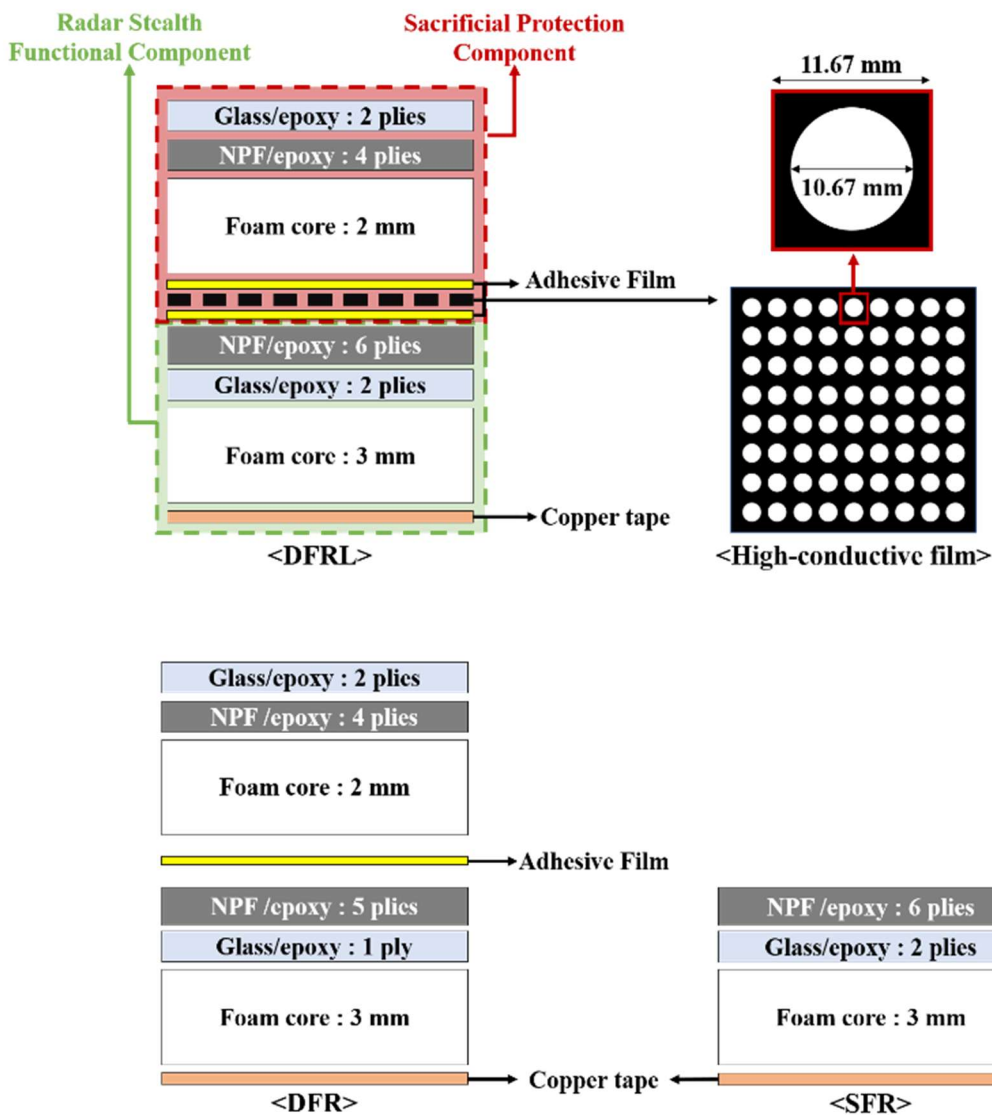


Fig. 6. Configuration of DFRL, DFR and SFR

Table 4: Stacking sequence of specimen

Specimens	Stacking Sequences
Double-slab foam RAS (DFR)	[GFRP-2 layers/NPF-4 layers/Foam-2 mm /NPF-5 layers /GFRP-1 layer/Foam-3 mm]
Double-slab foam RAS with lightning protection layer (DFRL)	[GFRP-2 layers/NPF-4 layers/Foam-2 mm/ Invar/NPF-6 layers/GFRP-2 layers/Foam-3 mm]
Single-slab foam RAS (SFR)	[NPF-6 layers/GFRP-2 layers/Foam-3 mm]

3.2 Fabrication

Specimens were prepared to confirm the damage and radar-absorbing performance after the lightning strike test. Fig. 7 shows the specimen fabrication process using an autoclave. First, based on the foamed RAS design described in Section 3.1, glass, NPF, foam core, high-conductive film, and adhesive film were stacked using the hand lay-up method. Next, curing accessories, such as peel ply, breather, and perforated release film, were stacked above the specimen, and a vacuum bag was attached using a sealant to create a vacuum inside the autoclave. The specimen was cured at a pressure of 3 bar at 120 °C for 2 h.

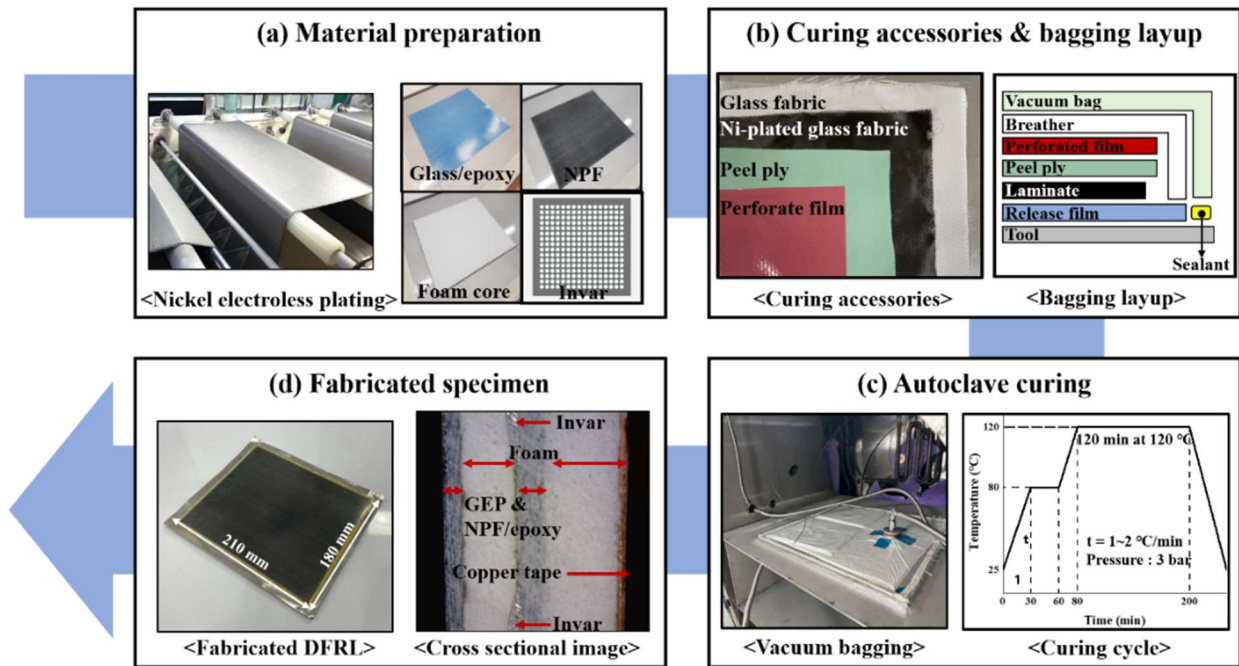


Fig. 7. Fabrication process flow of DFRL

We measured the radar-absorbing performance of specimens fabricated using the free space measurement equipment depicted in Fig. 8(a). Fig. 8(b) presents a graph summarizing the simulation and measurement results of radar-absorbing performance for each specimen. While the simulation and

measurement values do not perfectly align, it is evident that the radar-absorbing performance is effectively represented within the target frequency bandwidth. Although variations in material thicknesses from the design specifications may arise due to fabrication errors, the similarity observed between the simulated and measured values of radar-absorbing performance confirms the satisfactory fabrication of the specimens.

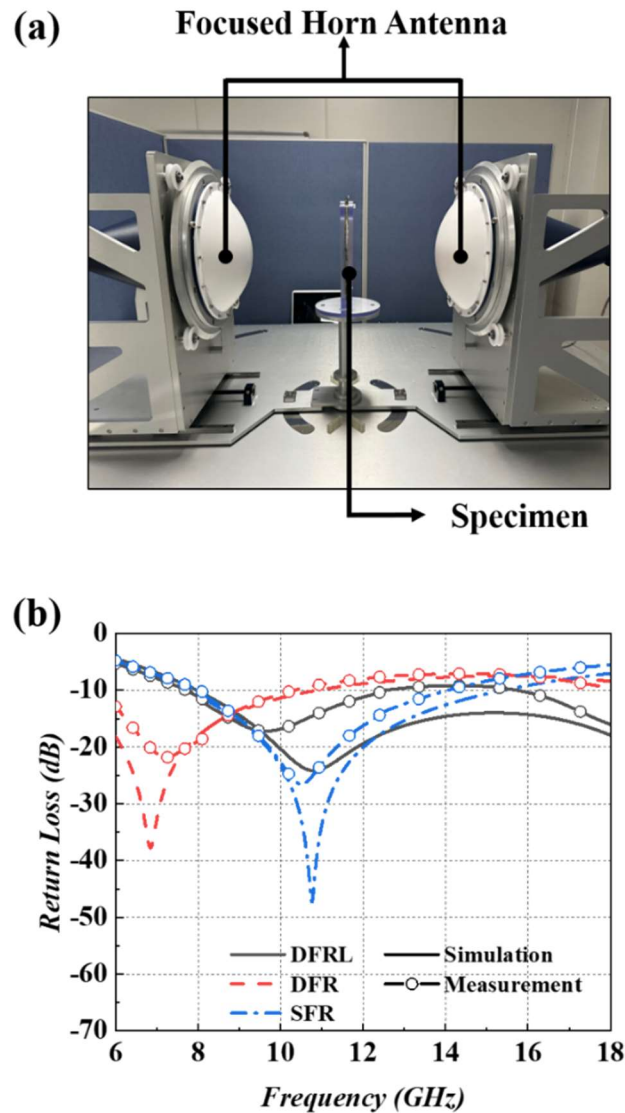


Fig. 8. (a) Free space measurement system, (b) Return loss simulation and measurement result of DFRL, DFR and SFR

4. Results and discussion

4.1 Evaluation of lightning strike impact damage

Lightning strike tests were conducted on the DFRL and DFR specimens (four of each type), each measuring 210 mm × 180 mm, as shown in Figs. 9(a) and 10(a), and the damages were compared. The damage to the specimen surface was assessed by considering fiber, matrix, and internal damage, as in^(51, 52). Binary images were created using binarization technology, as shown in Fig. 9(b) and 10(b),

to evaluate the damage to the specimen surface. Here, the white areas represent the damage caused by fiber damage or resin decomposition. The measurement results are summarized in Table 5.

The average area of damage on the DFR specimen surface is 9513.7 mm², excluding DFR #3, where the lightning impact was not properly applied due to the low conductivity of the specimen surface. In contrast, the average area of damage on the DFRL specimen surface is 5827.2 mm². This difference is because lightning rapidly dissipates as current by the high-conductive film, reducing damage on the specimens. Results from the micro-X-ray CT, as depicted in Figs. 9(c) and 10(c), confirm internal damage to the specimens. Although foam, owing to its similarity to air, may not be well observed with micro-X-ray CT, damage in composite laminates can be observed. Fig. 9(c) shows damage up to the 1st slab in DFR specimens subjected to a lightning strike. This suggests a significant impact on the specimen, causing delamination due to resin decomposition and fiber damage. In contrast, for the DFRL, in Fig. 10(c), damage, including fiber damage and delamination, occurs on the surface of the 2nd slab, whereas no severe damage is observed in the internal 1st slab. This indicates that the high-conductive film can suppress the damage occurring in the internal layers of the specimen from lightning strikes.

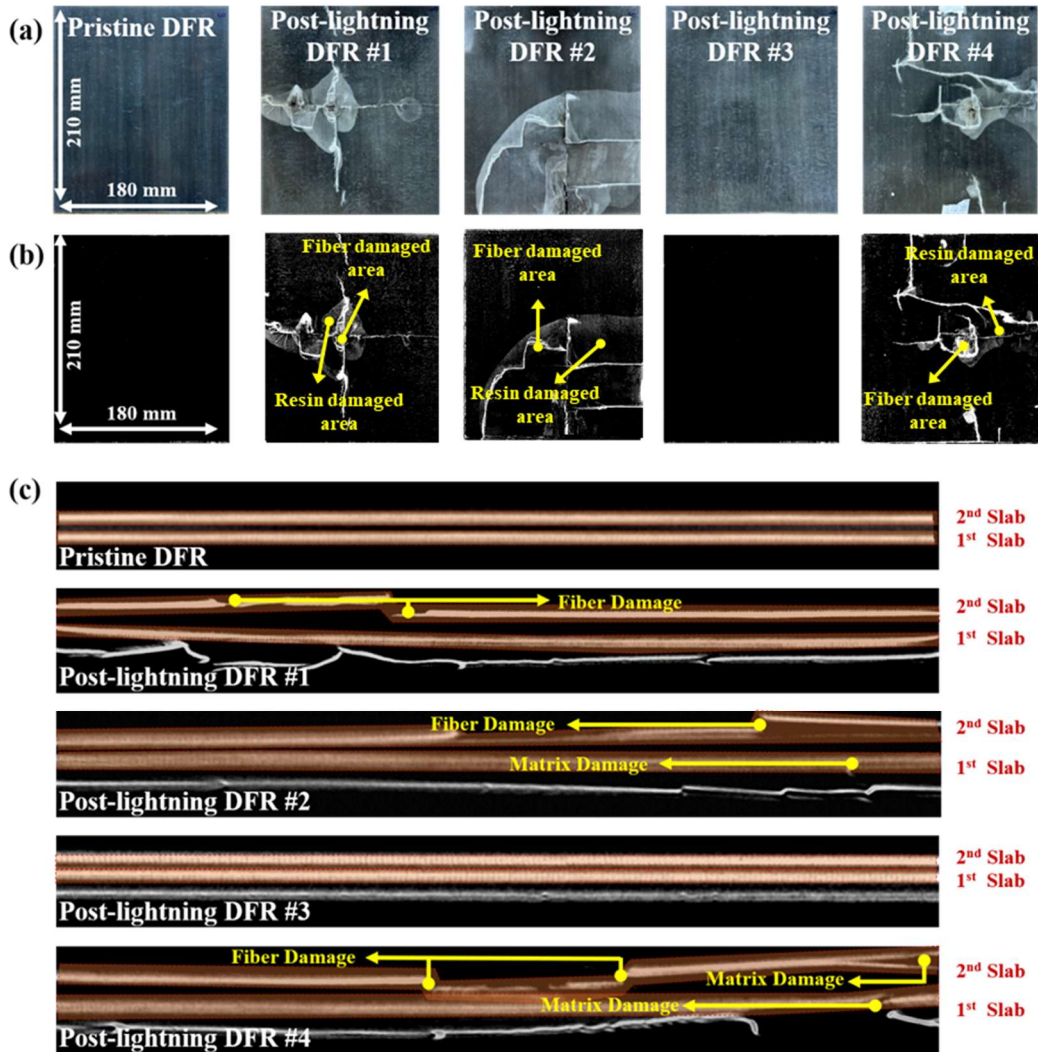


Fig. 9. Damage evaluation of DFR specimen after lightning strike test (a) Overhead view of the specimen before and after lightning strike test, (b) Image processing for measuring damage area, (c) Micro X-ray CT image

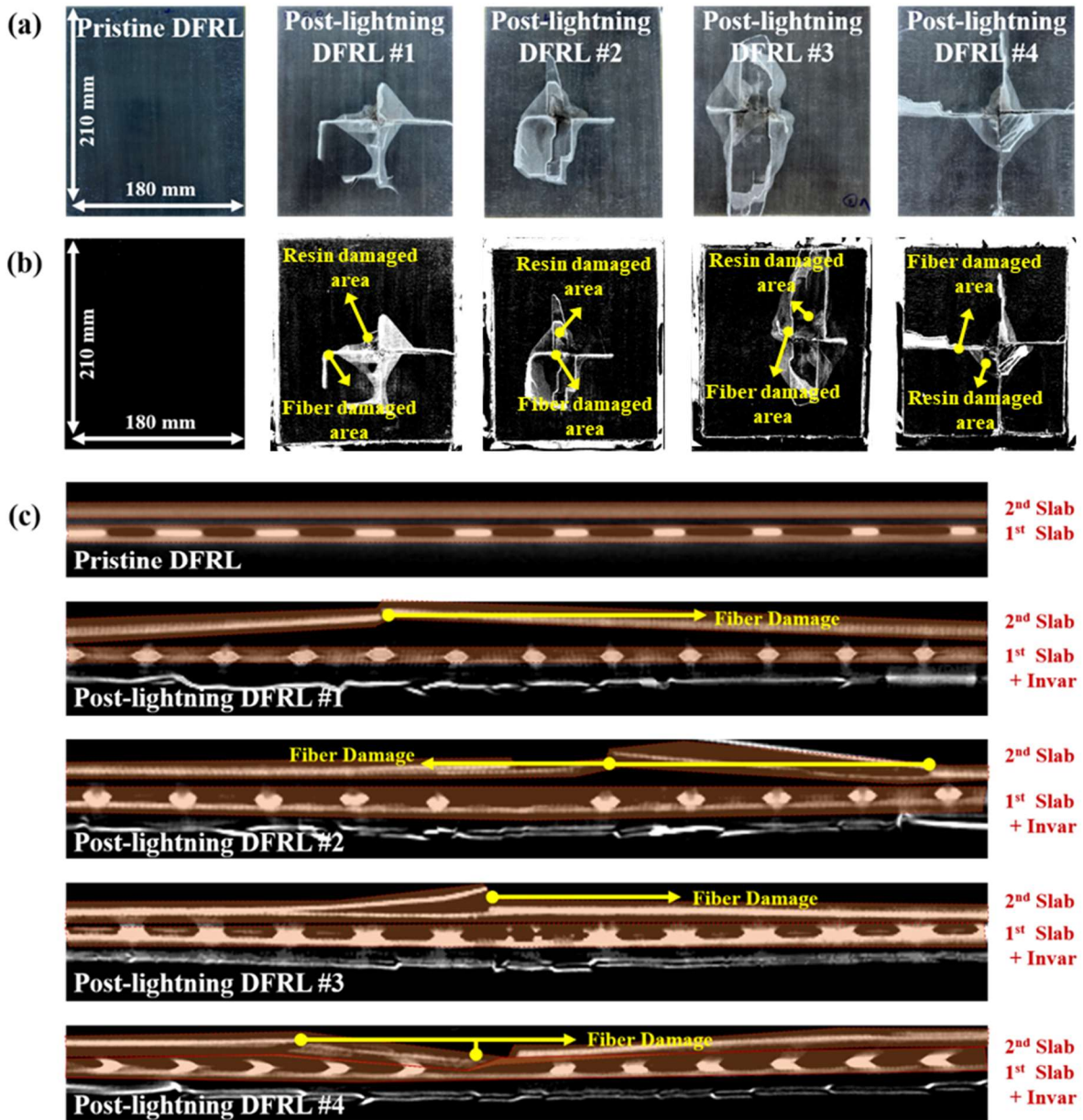


Fig. 10. Damage evaluation of DFRL specimen after lightning strike test (a) Overhead view of the specimen before and after lightning strike test, (b) Image processing for measuring damage area, (c) Micro X-ray CT image

Table 5: Summary of damage after lightning impact test

Specimens	Damage Area (mm ²)	Damage Type 1 st Slab	Damage Type 2 nd Slab
DFR #1	4836.4	-	Fiber Damage
DFR #2	17381.8	Matrix Damage	Fiber Damage
DFR #3	-	-	-
DFR #4	6323.0	Matrix Damage	Matrix & Fiber Damage
DFRL #1	3490.1	-	Fiber Damage
DFRL #2	5284.5	-	Fiber Damage
DFRL #3	9570.3	-	Fiber Damage
DFRL #4	4964.0	-	Fiber Damage

4.2 Radar stealth performance

4.2.1 Scanning image for radar absorption

Scanned return loss (S_{11}) measurements were conducted on the area subjected to a lightning strike to analyze the effect of lightning strikes on the radar-absorbing performance. Conventional return loss measurements only confirm if a lightning strike has affected the radar-absorbing performance of the entire specimen. However, the significance of this effect was not determined. Scanned S_{11} measurements enable the analysis of the damage caused to the RAS by a lightning strike and its effect on radar-absorbing performance. Therefore, it is widely used to confirm the radar-absorbing performance of RAS damaged by impact or lightning strikes⁽⁵²⁾.

This study confirmed the protective effect of a high-conductive film by comparing scanned S_{11} with and without the film. Four specimens with similar damage areas, namely DFR #1, DFR #4, DFRL #2, and DFRL #4, were selected for the scanned S_{11} measurements. S_{11} measurements were taken on the damaged area using a focused horn antenna, horizontally scanning at 10 mm intervals, as depicted in Fig. 11.

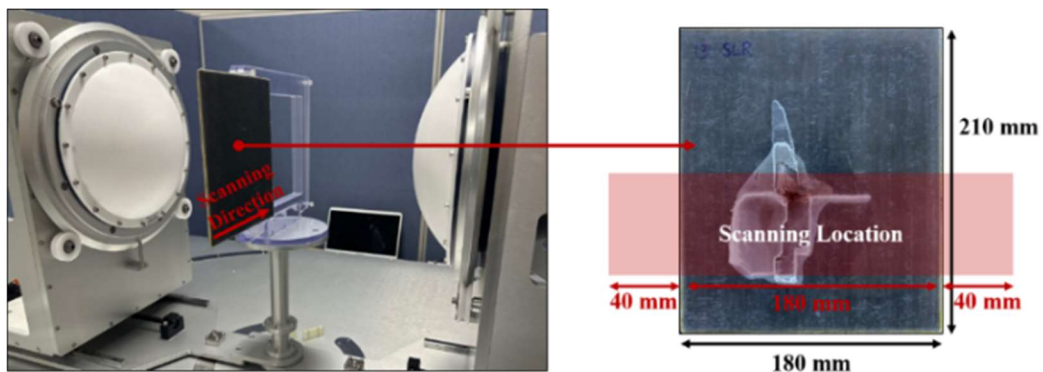


Fig. 11. Scanning S_{11} measurement equipment

First, the scanned S_{11} results were compiled for frequencies with the best radar-absorbing performance. Fig. 12 illustrates the difference in the scanned S_{11} between the DFR and DFRL specimens before and after the lightning strike test. The highest S_{11} differences observed for each specimen are as follows: DFR #1, 12.8%; DFR#4, 8.6%; DFRL#2, 7.3%; DFRL#4, 5.9%. Despite similar damage areas, DFR specimen has a higher S_{11} difference before and after the lightning strike than DFRL specimen.

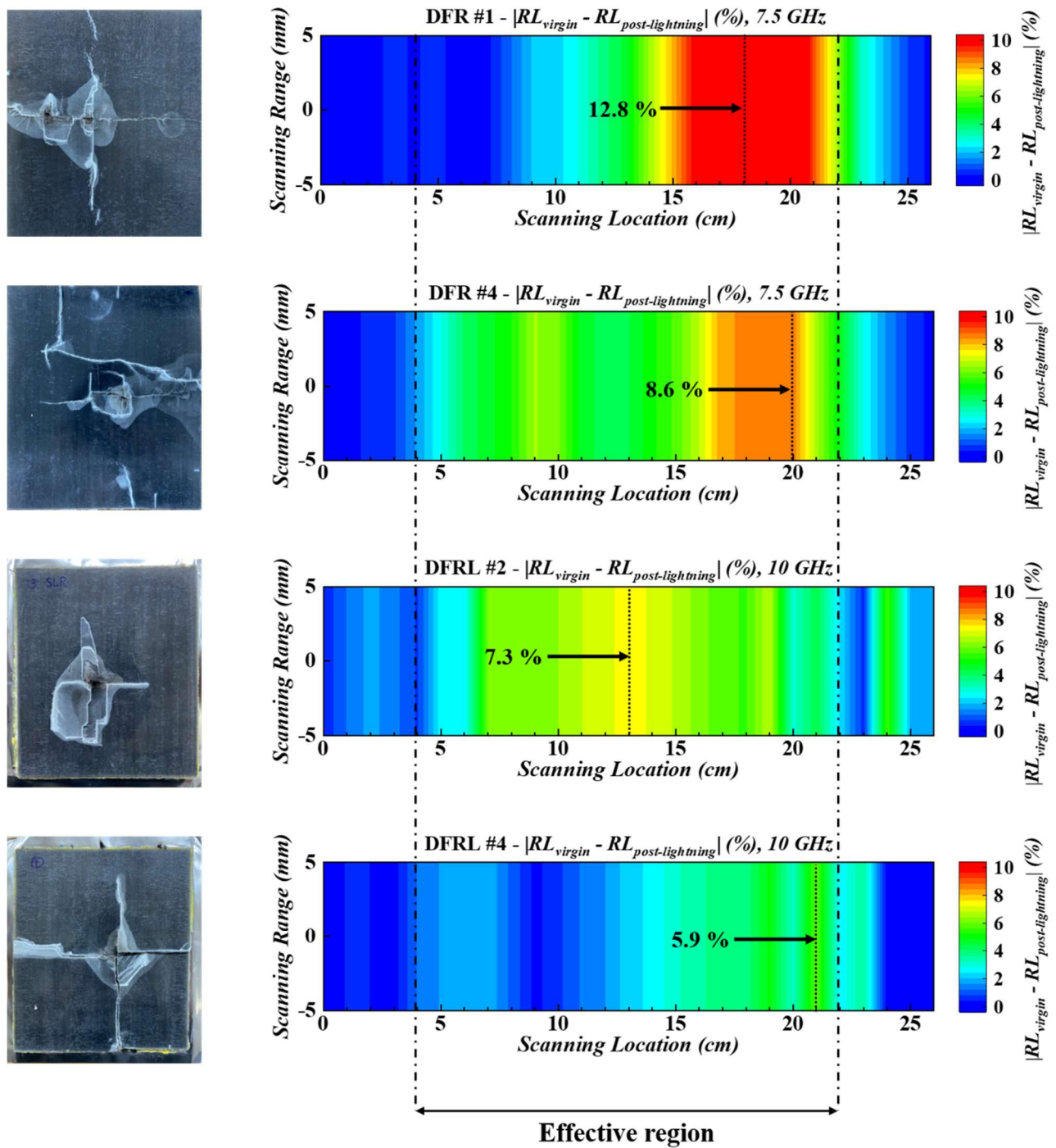


Fig. 12. Scanning result of absolute change in return loss (%) before and after lightning strike test

Fig. 13 summarizes the scanned S_{11} measurement results before and after the lightning strike tests for each target band of the DFR and DFRL. In Fig. 13(a), the average of absolute change in scanned S_{11} before and after lightning strikes at the center frequency (F_c) of the target frequency band is measured as 3.0% and 2.5% for DFR#1 and DFR#4 specimens, respectively. Furthermore, the highest average absolute changes in the scanned S_{11} within the target band are 6.2% and 6.3%, respectively. In contrast, in Fig. 13(b), the average absolute changes in scanned S_{11} before and after the lightning strike tests at the center frequency of the target band for DFRL#2 and DFRL#4 are lower than those for the DFR specimens and measured at 1.1% and 1.8%, respectively. Notably, the highest average absolute changes in the scanned S_{11} are 1.9% and 4.2%, respectively, lower than those observed for the DFR specimens. In DFR, this difference can be attributed to the internal damage incurred by the specimen due to the lightning strike, leading to significant variations in radar-absorbing performance. In contrast, in DFRL, the damage is concentrated on the sacrificial protection component because of the high-conductive film, resulting in a relatively maintained radar-absorbing performance.

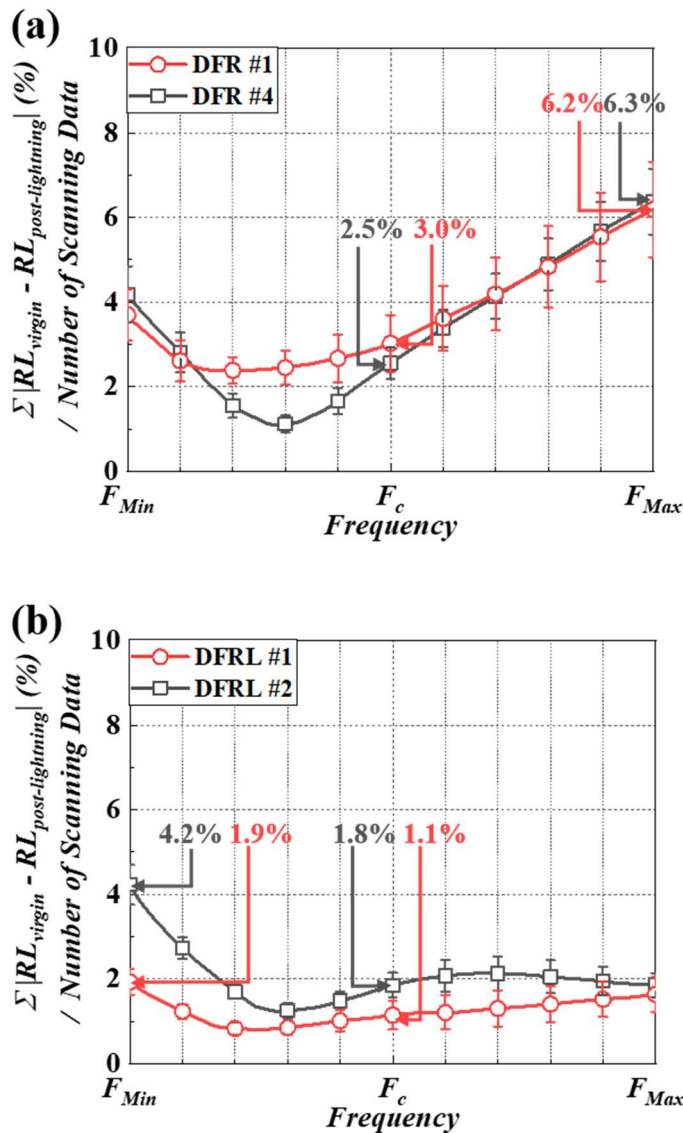


Fig. 13. Average of absolute change in return loss before and after the lightning strike test (a) DFR, (b) DFRL

4.2.2 Return loss

Fig. 14 compares the radar-absorbing performance before and after a lightning strike and examines the changes in the peak frequency and -10 dB bandwidth. The filled symbol represents the result of the virgin specimen, and the open symbol represents the result after the lightning strike. For DFR specimens, the peak frequency appears at 7.2 and 6.3 GHz before and after the lightning strike test, respectively, indicating a 12.5% change. In contrast, for DFRL specimens, the peak frequency appears at 9.6 and 10.0 GHz before and after the lightning strike test, respectively, representing a change of approximately 4.2%. Moreover, for DFR specimens, the -10 dB bandwidth was 5.8 to 10.3 GHz before the test but decreased to 5.8 to 8.6 GHz after the test, indicating the disappearance of radar-absorbing performance in the high-frequency range. However, for DFRL specimens, the -10 dB bandwidth was 7.7 to 12.5 GHz before the lightning strike test and extended to 7.7 to 18.0 GHz after the test, encompassing the -10 dB bandwidth of the virgin specimen. Lightning causes damage to the interior of the DFR specimens, increasing the total thickness of the specimens owing to delamination and shifting the -10 dB bandwidth towards lower frequencies. In contrast, the DFRL specimens experience minimal internal damage to the radar stealth functional components owing to the high-conductive film and maintain their performance even after the lightning strike test. The results confirm that the high-conductive film maintains its radar-absorbing performance even under a lightning strike.

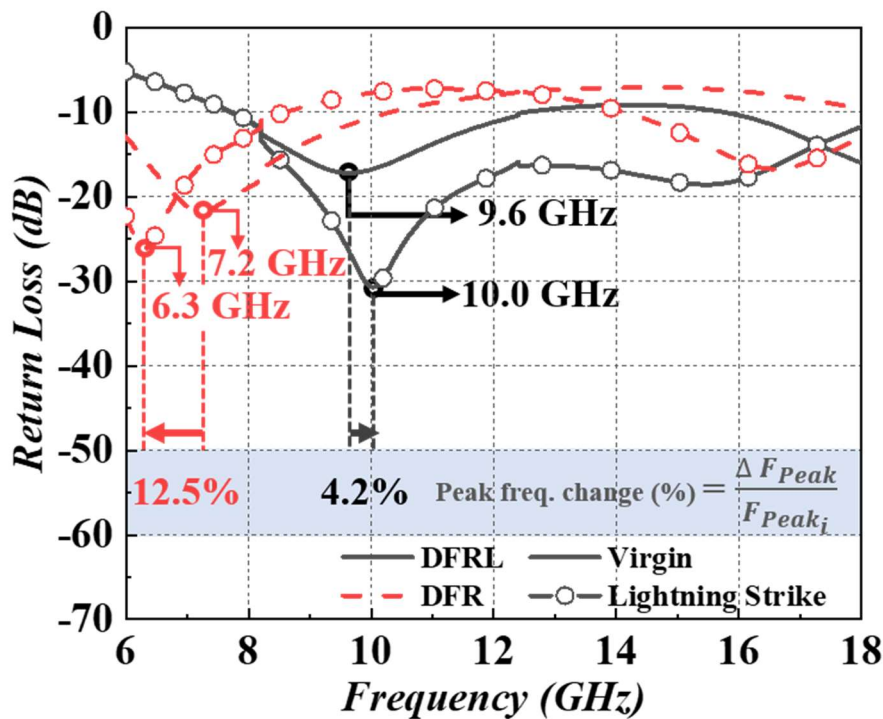


Fig. 14. Return loss measurement data of DFR and DFRL before and after the lightning strike test

5. Conclusions

We proposed foamed radar-absorbing sandwich composites with a high-conductive film to protect the RAS from lightning strikes and confirmed their protection performance. To protect the RAS from lightning strikes in the form of current and ensure radar-absorbing performance, a high-conductive film

was integrated into the RAS to design the DFRL. Image processing to analyze the surface damage caused by lightning strikes revealed that the damage area on the surface of the DFRL was 38.7% smaller than that on the DFR. Although minimal inertial damage was observed in 1st slab of the DFRL, inertial damage extending to the 1st slab was observed within the DFR using micro-X-ray CT. Moreover, for DFR specimens, the scanned S_{11} exhibited a maximum change of 6.3% in the radar-absorbing performance before and after the lightning strike test, and the -10 dB bandwidth decreased by 37.8% after the test. In contrast, the DFRL specimens showed a maximum change of 4.2% in the scanned S_{11} before and after the lightning strike test, and the -10 dB bandwidth confirmed covering the X-band and its surrounding bands, even after the lightning strike test. Thus, despite its thick construction, the proposed method effectively protects the RAS from lightning strikes.

참고문헌

- [1] Nam YW, Choi JH, Jang MS, Lee WJ and Kim CG. Radar-absorbing structure with nickel-coated glass fabric and its application to a wing airfoil model. *Compos Struct* 2017;180:507-512. doi: 10.1016/j.compstruct.2017.08.017.
- [2] Choi WH, Kwak BS, Noh YH, Yook JG, Kweon JH, Nam YW. Radar-absorbing nickel-coated fabric composite for wing-shaped structure in the X-band. *Compos Struct* 2020;239:111885. doi: 10.1016/j.compstruct.2020.111885.
- [3] Jin DH, Jang MS, Choi JH, Jang WH, Choi WH, Kim CG. Multi-slab hybrid radar absorbing structure containing short carbon fiber layer with controllable permittivity. *Compos Struct* 2021;273:114279. doi: 10.1016/j.compstruct.2021.114279.
- [4] Oh JH, Oh KS, Kim CG, Hong CS. Design of radar absorbing structures using glass/epoxy composite containing carbon black in X-band frequency ranges, *Compos Part B Eng* 2004;35(1):49-56. doi: 10.1016/j.compositesb.2003.08.011.
- [5] Wang C, Chen M, Lei H, Yao K, Li H, Wen W, Fang D. Radar stealth and mechanical properties of a broadband radar absorbing structure. *Compos Part B Eng* 2017;123:19-27. doi: 10.1016/j.compositesb.2017.05.005.
- [6] Panwar R, Lee JR. Recent advances in thin and broadband layered microwave absorbing and shielding structures for commercial and defense applications. *Funct Compos Struct* 2019;1(3):1-11. doi: 10.1088/2631-6331/ab2863.
- [7] Song TH, Choi WH, Shin JH, Lee WJ, Kim CG. Flexible design of dual-band radar-absorbing composites by controllable permittivity. *Int J Aeronaut Sp Sci* 2019;20(2):368-371. doi: 10.1007/s42405-019-00143-y.
- [8] Wang H, Zhu D. Design of Radar Absorbing Structure Using SiCf/Epoxy Composites for X Band Frequency Range. *Ind Eng Chem Res* 2018;57(6):2139- 2145. doi: 10.1021/acs.iecr.7b04905.
- [9] Yeswanth IVS, Jha K, Bhowmik S, Kumar R, Sharma S, Ilyas RA. Recent developments in RAM based MWCNT composite materials: A short review. *Funct Compos Struct* 2022;4(2):1-10. doi: 10.1088/2631-6331/ac5730.
- [10] Jang MS, Jang WH, Jin DH, Choi WH, Kim CG. Circuit-analog radar absorbing structures using a periodic pattern etched on Ni-coated glass fabric. *Compos Struct* 2022;281:115099. doi: 10.1016/j.compstruct.2021.115099.
- [11] Choi I, Lee D, Lee DG. Radar absorbing composite structures dispersed with nano-conductive particles. *Compos Struct* 2015;122:23-30. doi: 10.1016/j.compstruct.2014.11.040.
- [12] Xu C, Duan G, Xu W, Wang X, Huang Y, Zhang X, Zhu H, Wang BX. Thermally tunable vanadium-dioxide-based broadband metamaterial absorber with switchable functionality in the terahertz band. *Funct Compos Struct* 2023;5(2):1- 11. doi: 10.1088/2631-6331/acd490.

- [13] Choi JH, Nam YW, Jang MS, Kim CG. Characteristics of silicon carbide fiberreinforced composite for microwave absorbing structures. *Compos Struct* 2018;202:290–295. doi: 10.1016/j.compstruct.2018.01.081.
- [14] Baek SM, Lee WJ. A lightweight, flexible, and polarization-insensitive microwave absorbing honeycomb core using conductive losses in printed periodic pattern. *Compos Part A Appl Sci Manuf* 2024;180:2023108089. doi: 10.1016/j.compositesa.2024.108089.
- [15] Mazur V, Fisher BD, Gerlach JC. Lightning strikes to an airplane in a thunderstorm. *J Aircr* 1984;21(8):607–611. doi: 10.2514/3.45030.
- [16] Matsui T, Yamamoto K, Ogata J. Anomaly detection for wind turbine damaged due to lightning strike. *Electr Power Syst Res* 2022;209:2021107918. doi: 10.1016/j.epsr.2022.107918.
- [17] PavanFontanes C, Urbani M, Nguyen NC, Martinez-Sanchez M, Peraire J, Montanya J, Guerra-Garcia C. Aircraft Charging and its Influence on Triggered Lightning. *J Geophys Res Atmos* 2020;125(1):1–15. doi: 10.1029/2019JD031245.
- [18] Adyatma W, Hidayat S, Zoro R. Tropical Lightning Damage on Commercial Aircraft. *IEEE Aerosp Conf Proc*. March, 2021, p. 1–9. doi: 10.1109/AERO50100.2021.9438346.
- [19] Feraboli P, Miller M. Damage resistance and tolerance of carbon/epoxy composite coupons subjected to simulated lightning strike. *Compos Part A Appl Sci Manuf* 2009;40(6–7):954–967. doi: 10.1016/j.compositesa.2009.04.025.
- [20] Li Y, Li R, Lu L, Huang X. Experimental study of damage characteristics of carbon woven fabric/epoxy laminates subjected to lightning strike. *Compos Part A Appl Sci Manuf* 2015;79:1641175. doi: 10.1016/j.compositesa.2015.09.019.
- [21] Soulas F, Espinosa C, Lachaud F, Guinard S, Lepetit B, Revel I, Duval Y. A method to replace lightning strike tests by ball impacts in the design process of lightweight composite aircraft panels. *Int J Impact Eng* 2018;111:165–176. doi: 10.1016/j.ijimpeng.2017.09.007.
- [22] Wolfrum J, Schuster TJ, Körwien T, Effects of heavy lightning strikes on pristine and repaired carbon composite structures. *J Compos Mater* 2017;51(25):3491– 3504. doi: 10.1177/0021998317690445.
- [23] Wang FS, Yu XS, Jia SQ, Li P. Experimental and numerical study on residual strength of aircraft carbon/epoxy composite after lightning strike. *Aerosp Sci Technol* 2018;75:304–314. doi: 10.1016/j.ast.2018.01.029.
- [24] Lee J, Lacy TE, Pittman CU, Reddy JN. Numerical estimations of lightninginduced mechanical damage in carbon/epoxy composites using shock wave overpressure and equivalent air blast overpressure. *Compos Struct* 2019;224:111039. doi: 10.1016/j.compstruct.2019.111039.
- [25] Guo Y, Dong Q, Chen J, Yao X, Yi X, Jia Y. Comparison between temperature and pyrolysis dependent models to evaluate the lightning strike damage of carbon fiber composite laminates. *Compos Part A Appl Sci Manuf* 2017;97:10–18. doi: 10.1016/j.compositesa.2017.02.022.
- [26] Feraboli P, Kawakami H. Damage of carbon/epoxy composite plates subjected to mechanical impact and simulated lightning. *J Aircr* 2010;47(3):999–1012. doi: 10.2514/1.46486.
- [27] LeeGharghabi JH, Boushab D, Ricks TM, Lacy Jr TE, Pittman Jr CU, Mazzola MS, Velicki A. Artificial lightning strike tests on PRSEUS panels. *Compos Part B Eng* 2018;154:467–477. doi: 10.1016/j.compositesb.2018.09.016.
- [28] Yin JJ, Chang F, Li SL, Yao XL, Sun JR, Xiao Y. Experimental and Numerical Simulation Analysis of Typical Carbon Woven Fabric/Epoxy Laminates Subjected to Lightning Strike. *Appl Compos Mater* 2017;24(6):1353–1372. doi: 10.1007/s10443-017-9588-6.
- [29] Kamiyama S, Hirano Y, and Ogasawara T, Delamination analysis of CFRP laminates exposed to lightning strike considering cooling process. *Compos Struct* 2018;196:55–62. doi: 10.1016/j.compstruct.2018.05.003.
- [30] Kamiyama S, Hirano Y, Okada T, Ogasawara T. Lightning strike damage behavior of carbon

- fiber reinforced epoxy, bismaleimide, and polyetheretherketone composites. *Compos Sci Technol* 2018;161:107–114. doi: 10.1016/j.compscitech.2018.04.009.
- [31] Hirano Y, Katsumata S, Iwahori Y, Todoroki A. Artificial lightning testing on graphite/epoxy composite laminate. *Compos Part A Appl Sci Manuf* 2010;41(10):1461–1470. doi: 10.1016/j.compositesa.2010.06.008.
- [32] Yamashita S, Sonehara T, Takahashi J, Kawabe K, Murakami T. Effect of thin-ply on damage behaviour of continuous and discontinuous carbon fibre reinforced thermoplastics subjected to simulated lightning strike. *Compos Part A Appl Sci Manuf* 2017;95:132–140. doi: 10.1016/j.compositesa.2017.01.010.
- [33] Dong Q, Guo Y, Chen J, Yao X, Yi X, Ping L, Jia Y. Influencing factor analysis based on electrical-thermal-pyrolytic simulation of carbon fiber composites lightning damage. *Compos Struct* 2016;140:1–10. doi: 10.1016/j.compstruct.2015.12.033.
- [34] Foster P, Abdelal G, Murphy A. Quantifying the Influence of Lightning Strike Pressure Loading on Composite Specimen Damage. *Appl Compos Mater* 2019;26(1):115–137. doi: 10.1007/s10443-018-9685-1.
- [35] Ogasawara T, Hirano Y, Yoshimura A. Coupled thermal-electrical analysis for carbon fiber/epoxy composites exposed to simulated lightning current. *Compos Part A Appl Sci Manuf* 2010;41(8):973–981. doi: 10.1016/j.compositesa.2010.04.001.
- [36] Ma X, Scarpa F, Peng HX, Allegri G, Yuan J, Ciobanu R. Design of a hybrid carbon fibre/carbon nanotube composite for enhanced lightning strike resistance. *Aerosp Sci Technol* 2015;47:367–377. doi: 10.1016/j.ast.2015.10.002.
- [37] Kumar V, Yokozeki T, Okada T, Hirano Y, Goto T, Takahashi T, Ogasawara T. Effect of through-thickness electrical conductivity of CFRPs on lightning strike damages. *Compos Part A Appl Sci Manuf* 2018;114:429–438. doi: 10.1016/j.compositesa.2018.09.007.
- [38] Zhang J, Zhang X, Cheng X, Hei Y, Xing L, Li Z. Lightning strike damage on the composite laminates with carbon nanotube films: Protection effect and damage mechanism. *Compos Part B Eng* 2019;168:342–352. doi: 10.1016/j.compositesb.2019.03.054.
- [39] Guo M, Yi X, Liu G, Liu L. Simultaneously increasing the electrical conductivity and fracture toughness of carbon-fiber composites by using silver nanowiresloaded interleaves. *Compos Sci Technol* 2014;97:27–33. doi: 10.1016/j.compscitech.2014.03.020.
- [40] Wang B, Duan Y, Xin Z, Yao X, Abliz D, Ziegmann G. Fabrication of an enriched graphene surface protection of carbon fiber/epoxy composites for lightning strike via a percolating-assisted resin film infusion method. *Compos Sci Technol* 2018;158:51–60. doi: 10.1016/j.compscitech.2018.01.047.
- [41] Chakravarthi DK, Khabashesku VN, Vaidyanathan R, Blaine J, Yarlagadda S, Roseman D, Zeng Q, Barrera EV. Carbon fiber-bismaleimide composites filled with nickel-coated single-walled carbon nanotubes for lightning-strike protection. *Adv Funct Mater* 2011;21(13):2527–2533. doi: 10.1002/adfm.201002442.
- [42] Katunin A, Krukiewicz K, TurczynSul R, Łasica A, Bilewicz M. Synthesis and characterization of the electrically conductive polymeric composite for lightning strike protection of aircraft structures. *Compos Struct* 2017;159:773–783. doi: 10.1016/j.compstruct.2016.10.028.
- [43] Rehbein J, Wierach P, Gries T, Wiedemann M. Improved electrical conductivity of NCF-reinforced CFRP for higher damage resistance to lightning strike. *Compos Part A Appl Sci Manuf* 2017;100:352–360. doi: 10.1016/j.compositesa.2017.05.014.
- [44] Yokozeki T, Goto T, Takahashi T, Qian D, Itou S, Hirano Y, Ishida Y, Ishibashi M, Ogasawara T. Development and characterization of CFRP using a polyanilinebased conductive thermoset matrix. *Compos Sci Technol* 2015;117:277–281. doi: 10.1016/j.compscitech.2015.06.016.
- [45] Wang F, Ma X, Zhang Y, Jia S. Lightning damage testing of aircraft compositereinforced panels

- and its metal protection structures. *Appl Sci* 2018;8(10):1791. doi: 10.3390/app8101791.
- [46] Xia Q, Zhang Z, Mei H, Liu Y, Leng J. A double-layered composite for lightning strike protection via conductive and thermal protection. *Compos Commun* 2020;21:100403. doi: 10.1016/j.coco.2020.100403.
- [47] Zhu H, Fu K, Yang B, Li Y. Nickel-coated nylon sandwich film for combination of lightning strike protection and electromagnetic interference shielding of CFRP composite. *Compos Sci Technol* 2021;207:108675. doi: 10.1016/j.compscitech.2021.108675.
- [48] Lin W, Wang Y, Yousefpour K, Park C, and Kumar V. Evaluating the Lightning Strike Damage Tolerance for CFRP Composite Laminates Containing Conductive Nanofillers. *Appl Compos Mater* 2022;29(4):1537–1554. doi: 10.1007/s10443-022-10028-1.
- [49] Chu H, Xia Q, Zhang Z, Liu Y, and Leng J. Sesame-cookie topography silver nanoparticles modified carbon nanotube paper for enhancing lightning strike protection. *Carbon NY* 2019;143:204–214. doi: 10.1016/j.carbon.2018.11.022.
- [50] Choi WH, Kwak BS, Kweon JH, Nam YW, Radar-absorbing foam-based sandwich composite with electroless nickel-plated glass fabric. *Compos Struct* 2020;243:112252. doi: 10.1016/j.compstruct.2020.112252.
- [51] Jang MS, Choi JH, Jang WH, Nam YW, Kim CG, Influence of lightning strikes on the structural performance of Ni-glass/epoxy radar-absorbing structures. *Compos Struct* 2020;245:2019112301. doi: 10.1016/j.compstruct.2020.112301.
- [52] Jeong GW, Noh YW, Choi WH, Shin JH, Kweon JH, Yook JG, Nam YW. Electromagnetic-mechanical repair patch of radar-absorbing structure with electroless nickel-plated glass fabric damaged by lightning strike. *J Compos Mater* 2021;55(7):989–1002. doi: 10.1177/0021998320961558.
- [53] Choe HS, Lee JS, Kweon JH, Nam YW, Choi WH. High-performance microwave absorption heating honeycomb sandwich composite with electroless nickel-plated glass fiber. *Compos Struct* 2022;283:2021115138. doi: 10.1016/j.compstruct.2021.115138.
- [54] Jang MS, Choi JH, Jang WH, Nam YW, Kim CG. Effects of dot-type electroless nickel plating on the mechanical properties of glass/epoxy used for radar-absorbing structures. *Compos Struct* 2021;257:2020113165. doi: 10.1016/j.compstruct.2020.113165.
- [55] Lightning qualification test techniques for aerospace vehicles and hardware, MILSTD-1757A, 20 July 1983.